Dynamical Heterogeneity near Glass Transition Temperature under Shear Conditions

Taiki Hoshino, So Fujinami, Tomotaka Nakatani, and Yoshiki Kohmura

Phys. Rev. Lett. **124**, 118004 — Published 17 March 2020

DOI: 10.1103/PhysRevLett.124.118004

Dynamical Heterogeneity near Glass-Transition Temperature under Shear Conditions

Taiki Hoshino*, So Fujinami, Tomotaka Nakatani, and Yoshiki Kohmura

RIKEN SPring-8 Center, 1-1-1 Kouto, Sayo-cho, Sayo-gun, Hyogo 679-5148, Japan

Abstract

We experimentally studied the shear effect on dynamical heterogeneity near glass-transition temperature. X-ray photon correlation spectroscopy was utilized to study the dynamics of polyvinyl acetate with tracer particles near its glass-transition temperature, to determine the local shear rate from the anisotropic behavior of the time autocorrelation function, and to calculate the dynamical heterogeneity using higher-order correlation function. The obtained results show a decrease in the dynamical heterogeneity and faster dynamics with increasing shear rate. This is the first experimental result that proved the predictions by previous molecular dynamics simulations.

Glass transition is a ubiquitous, well-studied phenomenon, occurring in metals, polymers, molecular and ionic liquids, and colloidal dispersions [1,2]. However, many unsolved problems remain, particularly concerning glassy state dynamics. Upon cooling, liquid viscosity drastically increases near its glass-transition temperature T_g, mostly due to the cooperative movement of molecules, rather than the individual thermal molecular motion. In the glassy state, regions with a low and a high mobility coexist and molecules move cooperatively in the dynamically-correlated region; this is known as "dynamical heterogeneity" (DH) [3,4].

Shear can affect DH. Using molecular dynamics (MD) simulations, Yamamoto and Onuki reported that the DH of a two-component Lennard-Jones liquid decreased upon applying shear to the supercooled state, and demonstrated that the viscosity decreased with increased shear rate $\dot{\gamma}$ [5,6]. Subsequently, there have been various simulations investigating DH under shear in the glassy state and in jamming systems [7-10]. On the other hand, experiments were performed only near the jamming transition on the highly concentrated particle systems [11, 12]. Both of glass transition and jamming transition involve solidification and a disordered particle arrangement, so they are often treated similarly. However, jamming transition is an athermal phenomenon, whereas glass transition involves thermal motion, and they are now regarded as distinct phenomena [13]. To our knowledge, the research in this paper shows the first experimental result to investigate the influence of shear on the DH near T_g.

X-ray photon correlation spectroscopy (XPCS) allows microscopic observation based on the temporal fluctuation of the scattering intensity of partially-coherent x-rays [14]. Previous XPCS studies of the dynamics of samples below $1.1T_\mathrm{g} - 1.2T_\mathrm{g}$ revealed that the motion of tracer particles become hyperdiffusive by analyzing the time autocorrelation function of scattered intensity [15-17]. Furthermore, Conrad *et al.* analyzed higher-order correlations in the scattering data and found that the DH increased close to and below $1.12T_\mathrm{g}$ [18]. XPCS are also carried out to elucidate the dynamical behavior under shear. To exemplify, Busch *et al.* and Burghardt *et al.*, observed Brownian motion under Poiseuille flow using colloidal suspensions [19] and under homogeneous flow between plates [20], respectively. Westermeier *et al.* observed the transient static structural changes and dynamical changes of soft colloidal liquids due to three dimensional shear with plate-plate and Couette geometry [21].

In this study, the dynamics of polyvinyl acetate (PVAc) under shear was investigated using XPCS at near T_g with dispersed silica tracer particles, and $\dot{\gamma}$-DH relationship was investigated. The experimental sample comprised 120-nm-diameter silica particles (Nissan Chemicals, Japan) dispersed in a PVAc ($M_\mathrm{n} = 3800$, $M_\mathrm{w}/M_\mathrm{n} = 1.18$) matrix, where M_n and M_w are the number-average and weight-averaged molecular weight, respectively, the T_g of which was 298 K, as measured by differential scanning calorimetry (FP90/FP84HT, Mettler Toledo, U.S.). The silica particles were homogeneously dispersed at a concentration of ~1 vol%, and the inter-particle interaction was negligible within the measured q-range, as confirmed by small-angle x-ray scattering measurements performed at BL05XU beamline in SPring-8. Fig. 1 schematically illustrates the experimental setup. The sample was sandwiched between a silicon substrate and a cylindrical stainless-steel rod ($r = 4$ mm), which was 3 mm thick in the beam direction. The minimum gap at the center was 173 μm, which was measured by scanning with the x-ray beam. The center of the sample, where the substrate and cylindrical surface were closest, was irradiated with x-rays. A gas flow with a low rate controlled the temperature of the entire sample cell. The XPCS measurements were performed at 336 K, which is lower than $1.2T_\mathrm{g}$ (358 K). A piezo stage moved the silicon substrate at a constant speed (V) to apply shear. Force sensors monitored the vertical and horizontal stresses applied to the rod. Although the stress changed at the initiation of substrate movement, x-ray irradiation after sufficiently long elapsed time guaranteed the constant stress during measurement.

The XPCS measurements were conducted at a beamline BL29XUL at SPring-8 [22]. The undulator source and Si(111) monochromator were tuned to 12.40 keV and higher harmonic x-rays were removed by Pt-coated mirrors. The sample was irradiated with partially-coherent x-rays obtained by passing the beam through 20×20 μm^2 slits. The scattered x-rays were detected using an EIGER 1M 2D detector (Dectris, Switzerland) mounted ~5.4 m downstream of the sample. The measured beam size at the sample position was $W_\mathrm{x} = 10.6\ \mu\mathrm{m}$ (horizontal direction) and $W_\mathrm{y} = 9.7\ \mu\mathrm{m}$ (vertical direction), as measured by a wire scan method, and the measured beam profiles were expressed as $I(x) \propto \exp[-x^2/W_\mathrm{x}^2]$ (horizontal direction) and $I(y) \propto \exp[-y^2/W_\mathrm{y}^2]$ (vertical direction).

In the XPCS measurements, the fluctuation of the scattering intensity $I(\mathbf{q},t)$ at a scattering vector $\mathbf{q}$ was obtained over a time series t, and the intensity time autocorrelation function $g_2(\mathbf{q},t)$ was evaluated as

$$g_2(\mathbf{q},t) = \langle I(\mathbf{q},t')I(\mathbf{q},t'+t)\rangle / \langle I(\mathbf{q},t')\rangle^2. \quad (1)$$

Under shear conditions, $g_2(\mathbf{q},t)$ behaved anisotropically as shown in Fig. 2. Fig.2 shows plots of $[g_2(q_{//},t)-1]/\beta$ and $[g_2(q_\perp,t)-1]/\beta$, where β is the speckle contrast, at different values of $q(=q_{//}=q_\perp)$ and $V = 0.10\ \mu\mathrm{m\,s^{-1}}$ in the range of $\pm 15^\circ$, where $q_{//}$ and $q_\perp$ are the scattering wave vectors parallel and perpendicular to the shear direction, respectively. For all measured q values, $g_2(q_{//},t)$ exhibited faster relaxation than $g_2(q_\perp, t)$. Following these notations, we can derive the local $\dot{\gamma}$ at the irradiated position as follows.

The Siegert relationship relates $g_2(\mathbf{q}, t)$ to the intermediate scattering function $g_1(\mathbf{q}, t)$ [23];

$$g_2(\mathbf{q}, t) = 1 + \beta|g_1(\mathbf{q}, t)|^2, \tag{2}$$

where β~0.05 in these experiments and is similar in both directions. Busch *et al.* expresses $g_1(\mathbf{q}, t)$ under shear as follows [19]:

$$|g_1(\mathbf{q}, t)|^2 = |g_{1,\mathrm{D}}(\mathbf{q}, t)|^2 \cdot |g_{1,\mathrm{S}}(\mathbf{q}, t)|^2 \cdot |g_{1,\mathrm{T}}(\mathbf{q}, t)|^2, \tag{3}$$

where $g_{1,\mathrm{D}}(\mathbf{q}, t)$, $g_{1,\mathrm{S}}(\mathbf{q}, t)$, and $g_{1,\mathrm{T}}(\mathbf{q}, t)$ correspond to the particle diffusion, shear deformation, and particle transit through the scattering volume, respectively [24]. $g_{1,\mathrm{T}}(\mathbf{q}, t)$ is caused by the particles flowing into and replacing the existing particles in the scattering volume in the colloidal suspension. This $g_{1,\mathrm{T}}(\mathbf{q}, t)$ was neglected, since its time scale is more than ten times longer than the other time scale in the measured q range. Since $g_{1,\mathrm{S}}(\mathbf{q}, t) = 1$ perpendicular to the shear direction [19,24]:

$$|g_1(q_\perp, t)|^2 = |g_{1,\mathrm{D}}(q_\perp, t)|^2. \tag{4}$$

Similarly, the contribution in the parallel direction to the shear is:

$$|g_1(q_{//}, t)|^2 = |g_{1,\mathrm{D}}(q_{//}, t)|^2 \cdot |g_{1,\mathrm{S}}(q_{//}, t)|^2. \tag{5}$$

The diffusion term is conventionally expressed using stretched or compressed exponential functions:

$$|g_{1,\mathrm{D}}(\mathbf{q}, t)|^2 = \exp[-2(\Gamma t)^\alpha], \tag{6}$$

where Γ is the relaxation rate and α is the stretched or compressed exponent. According to Fuller *et al.*, the shear term can be expressed as

$$|g_{1,\mathrm{S}}(q_{//}, t)|^2 = \left|\int_0^{W_y} I(y)\exp(-i\,\dot{\gamma}\, q_{//} y t)dy\right|^2 = \exp\left(-\frac{1}{2}q_{//}^2\dot{\gamma}^2 W_y^2 t^2\right) \tag{7}$$

where $I(y)$ is the intensity profile perpendicular to the shear direction [25].

When $\dot{\gamma}/\Gamma \ll 1$, the decrement of viscosity induced by shear occurs isotopically, and the diffusion motion accelerated isotopically, to give the relationship of $g_{1,\mathrm{D}}(q_\perp, t) = g_{1,\mathrm{D}}(q_{//}, t)$ [6,7,11]. Using these relations, $g_2(q_\perp, t)$ and $g_2(q_{//}, t)$ are expressed as follows:

$$g_2(q_\perp, t) = 1 + \beta\exp[-2(\Gamma t)^\alpha] \tag{8}$$

$$g_2(q_{//}, t) = 1 + \beta\exp[-2(\Gamma t)^\alpha] \cdot \exp\left(-\frac{1}{2}q_{//}^2\dot{\gamma}^2 W_y^2 t^2\right)\ . \tag{9}$$

Using these relations, Γ and α were obtained by fitting $g_2(q_\perp, t)$ with Eq. (8). Subsequently, $g_2(q_{//}, t)$ at various $q_{//}$ values were simultaneously fitted with Eq. (9), using the common fitting parameter, $\dot{\gamma}$. These analyses gave the local $\dot{\gamma}$ in the irradiated volume. As shown in Fig. 2, the results of fitting agree well with the measured data, giving $\dot{\gamma} = 0.95 \times 10^{-3}\ \mathrm{s}^{-1}$ [26], and the calculated $[|g_{1,\mathrm{S}}(q_{//}, t)|^2 - 1]/\beta$ are depicted to explicitly show the effect of shear term. $g_2(q_{//}, t)$ showed a little hump in the baseline in most of the measured q-range, which could have arose from the angular deviation between the shear direction in the experiment and the slicing direction in the analysis [24]. We applied the same analysis to other data measured with different values of V.

Fig. 3(a) shows the measured $[g_2(q_\perp, t) - 1]/\beta$ curves at $q_\perp = 9.76 \times 10^{-2}\ \mathrm{nm}^{-1}$ for various values of $\dot{\gamma}$, which are representative of the $\dot{\gamma}$-dependence of $g_2(q_\perp, t)$. Note that the observed $g_2(q_\perp, t)$ and $g_2(q_{//}, t)$ (Fig. 3(a)), and relaxation rate at various $q_\perp$ and $q_{//}$ (Fig. 3(b)) for $\dot{\gamma} = 0\ \mathrm{s}^{-1}$, were almost identical which guaranteed that our measurements have no anisotropic systematic error. The measured $g_2(q_\perp, t)$ curves were well-fitted by Eq. (8) with Γ and α with q dependence. The derived Γ as a function of $q_\perp$ is shown in Fig. 3(b) which is proportional to $q_\perp$. The derived α declined from around 2 to around 1 by increasing $q_\perp$. Similar features of the q-dependence of Γ and α for the hyperdiffusive behavior have been reported for the dynamics near T_g [15-17]. Using the proportional constant A in $\Gamma = Aq_\perp$, Fig. 4 shows $\dot{\gamma}$-dependence of A^{-1}. A^{-1} decreases with increasing $\dot{\gamma}$ with a power law function of $A^{-1} \propto \dot{\gamma}^{-0.71 \pm 0.07}$, where the power law exponent is obtained by fitting considering the error weights. Conversely, clear $\dot{\gamma}$-dependence of α was not observed.

The above discussion was "averaged" over time. Hereafter, we move on to discussion about time variance of time-autocorrelation functions to examine DH, In previous studies, the two-time correlation function [27,28]

$$C_I(q_\perp, t_1, t_2) = \frac{\langle I_p(q_\perp, t_1) I_p(q_\perp, t_2) \rangle_\Psi}{\langle I_p(q_\perp, t_1) \rangle_\Psi \langle I_p(q_\perp, t_2) \rangle_\Psi} \tag{10}$$

is calculated, where $\langle \cdot \rangle_\Psi$ denotes the average over pixels within $q_\perp \pm \Delta q_\perp$. Here, t_2 was replaced with $t_1 + \varDelta t$. Figs. 5(a)-(d) show plots of $C_I(q_\perp, t_1, \varDelta t)$ at $q_\perp = 9.76 \times 10^{-2}\ \mathrm{nm}^{-1}$ for various values of $\dot{\gamma}$, to show the $\dot{\gamma}$-dependency of C_I. The relaxation time scale of C_I was clearly faster as $\dot{\gamma}$ increased. We, however, recognize that $\dot{\gamma}$ dependence of the fluctuation of relaxation time, e.g. $\varDelta t$ value of $C_I = 1.02$, is not obvious. We here quantitatively evaluate the fluctuation of C_I by calculating its normalized variance [29]:

$$\chi(q_{\perp}, t) = \frac{<C_I^2(q_{\perp}, t_1, \varDelta t)>_{t_1} - <C_I(q_{\perp}, t_1, \varDelta t)>_{t_1}^2}{<C_I(q_{\perp}, t_1, \varDelta t = 0)>_{t_1}^2}. \tag{11}$$

χ exhibits a peak around the $g_2(q_{\perp}, t)$ inflection point. The peak height is proportional to the variance of the characteristic relaxation time. χ is proportional to the volume integral of the spatial correlation of the dynamics and corresponds to the so-called dynamical susceptibility χ_4 studied in various simulation and theoretical researches [30-32]. The experimentally-measured variance $\chi(q_{\perp}, t)$ was affected by the statistical noise owing to the finite number of pixels n_{p} used. Thus, we applied a correction procedure to $\chi(q_{\perp}, t)$ by an extrapolation to the case of $1/n_{\mathrm{p}} = 0$ $(n_{\mathrm{p}} \rightarrow \infty)$ [31,33]. Fig. 6 shows the corrected $\chi(q_{\perp}, t)$ plots at $q_{\perp} = 9.76 \times 10^{-2}\ \mathrm{nm}^{-1}$ as a function of $\dot{\gamma}$. As $\dot{\gamma}$ increased, the height of χ (χ^*) and therefore the fluctuation of C_I, clearly decreased, and the peak position (τ^*) shifted to shorter time constant, indicating the faster dynamics.

Similar measurements were performed as function of $\dot{\gamma}$ (Fig. 7(a)) and τ^* (Fig. 7(b)) at $q_{\perp} = 9.76 \times 10^{-2}\ \mathrm{nm}^{-1}$. As $\dot{\gamma}$ increased, χ^* decreased, indicating that the degree of fluctuation of the dynamics decreased. Fitting χ^* to $\chi^* \propto \dot{\gamma}^{-\mu}$ gave $\mu = 0.30 \pm 0.07$. τ^* also decreased as $\dot{\gamma}$ increased, indicating that the dynamics became faster. The power law $\tau^* \propto \dot{\gamma}^{-\nu}$ gives $\nu = 0.72 \pm 0.11$. These dependences approximated by power law functions are consistent with MD simulations, suggesting that the DH decreases and the dynamics become faster with increasing $\dot{\gamma}$. Similar results were obtained at different values of q $(8.76 \times 10^{-2} < q < 10.76 \times 10^{-2}\ \mathrm{nm}^{-1})$ [34]. The average of these results gives $\mu = 0.20 \pm 0.03$ and $\nu = 0.73 \pm 0.06$.

We investigate whether the shear rate may fluctuate, because fluctuation of $\dot{\gamma}$ could affect χ^* and τ^*. $\dot{\gamma}$ as a function of t_1 can be derived from $C_I(q_{\perp}, t_1, \varDelta t)$ and $C_I(q_{//}, t_1, \varDelta t)$ using functions in Eqs. (8) and (9) in a similar manner to that used for $g_2(q_{\perp}, t)$ and $g_2(q_{//}, t)$ to derive $\dot{\gamma}$. By such analysis, we came to conclude that the standard deviation of $\dot{\gamma}$ $(\varDelta\dot{\gamma})$ is approximately 12 % by averaging over various conditions of $\dot{\gamma}$, and there is no clear correlation between $\varDelta\dot{\gamma}$ and $\dot{\gamma}$. In the previous paragraph, we showed that χ^* and τ^* have $\dot{\gamma}$-dependence, which, therefore, should not be related to $\varDelta\dot{\gamma}$. $\varDelta\dot{\gamma}$, on the other hand, may be related to the noise observed in the calculated χ^* and τ^*.

The 120-nm-diameter particles used were considerably larger than the molecular size of liquids - the particle size typically used in MD simulations. Therefore, our μ and ν values would not necessarily match MD simulation values. However, it is valuable to compare. The obtained value of μ (= 0.20) is fairly close to 0.26, the value determined for a supercooled liquid by Mizuno and Yamamoto [8] and is sufficiently close to 0.3, the value obtained for a jamming system by Nordstrom *et al.* using video microscopy [12]. However, it is smaller than the values of 0.4–0.6 reported for a 2D Lennard-Jones amorphous solid by Tsamados based on MD simulations [10]. The obtained value of ν (= 0.73) is near the values of approximately 0.8 reported by Mizuno and Yamamoto and other MD simulations [5,7] and confocal microscopy of colloidal glasses [11] although it is larger than 0.63, the value reported by Tsamados. The particle size and concentration dependence remain intriguing open questions.

There may be interesting findings related to the q-dependence of μ and ν which will be enabled by enlarging the range of q like the previous reports [29,33,35,36]. However, there are problems of small number of pixels in the lower-q region and very low statistics in the higher-q region. The q-dependence of μ and ν also remains open questions.

We investigated the fluid dynamics of PVAc near its T_{g} by XPCS method using particles as the marker. The local $\dot{\gamma}$ at the irradiated position was determined from the anisotropic behavior of $g_2(\mathbf{q}, t)$, and the DH was examined for various values of $\dot{\gamma}$ using the higher-order correlation functions. We observed a much reduced DH and a faster dynamics when $\dot{\gamma}$ is increased. Those $\dot{\gamma}$-dependencies were fitted using power law functions, and similar power law exponents were obtained as in the previous reports. In this paper, we performed an experiment on a simple model system containing low-molecular-weight PVAc and dilute dispersed particles. This approach is powerful and applicable to more complex systems containing high-molecular-weight polymers and higher concentration of particle dispersions. Such study has a huge potential to reveal fundamental mechanism of dynamics occurring in non-equilibrium states.

ACKNOWLEDGMENTS

The XPCS experiments at beamline BL29XUL were performed with the approval of RIKEN (Proposal Nos. 20170026 and 20180027). The work of T.H., S.F., and T.N. was partially supported by the ImPACT Program of the Council for Science, Technology and Innovation (Cabinet Office, Government of Japan). T.H. acknowledges JST PRESTO for funding the project “Molecular technology and creation of new functions” and JSPS KAKENHI (Grant No. JP18K05226).

REFERENCES

[1] C. A. Angell, Science **267**, 1924 (1995).

[2] L. Berthier and G. Biroli, Reviews of Modern Physics **83**, 587 (2011).

[3] M. D. Ediger, Annu Rev Phys Chem **51**, 99 (2000).

[4] L. Berthier, G. Biroli, J.-P. Bouchaud, L. Cipelletti, and W. van Saarloos, *Dynamical Heterogeneities in Glasses, Colloids, and Granular Media* (Oxford University Press, Oxford, 2011).

[5] R. Yamamoto and A. Onuki, Physical Review Letters **81**, 4915 (1998).

[6] R. Yamamoto and A. Onuki, Physical Review E **58**, 3515 (1998).

[7] K. Miyazaki, D. R. Reichman, and R. Yamamoto, Phys Rev E Stat Nonlin Soft Matter Phys **70**, 011501 (2004).

[8] H. Mizuno and R. Yamamoto, J Chem Phys **136**, 084505 (2012).

[9] C. Heussinger, P. Chaudhuri, and J.-L. Barrat, Soft Matter **6**, 3050 (2010).

[10] M. Tsamados, Eur Phys J E Soft Matter **32**, 165 (2010).

[11] R. Besseling, E. R. Weeks, A. B. Schofield, and W. C. Poon, Phys Rev Lett **99**, 028301 (2007).

[12] K. N. Nordstrom, J. P. Gollub, and D. J. Durian, Phys Rev E Stat Nonlin Soft Matter Phys **84**, 021403 (2011).

[13] A. Ikeda, L. Berthier, and P. Sollich, Phys Rev Lett **109**, 018301 (2012).

[14] G. Grubel, A. Madsen, and A. Robert, *Soft Matter Characterization* (Springer-Verlag Berlin Heidelberg, 2008).

[15] C. Caronna, Y. Chushkin, A. Madsen, and A. Cupane, Phys Rev Lett **100**, 055702 (2008).

[16] H. Guo, G. Bourret, M. K. Corbierre, S. Rucareanu, R. B. Lennox, K. Laaziri, L. Piche, M. Sutton, J. L. Harden and R. L. Leheny, Phys Rev Lett **102**, 075702 (2009).

[17] T. Hoshino, D. Murakami, Y. Tanaka, M. Takata, H. Jinnai, and A. Takahara, Phys Rev E Stat Nonlin Soft Matter Phys **88**, 032602 (2013).

[18] H. Conrad, F. Lehmkuhler, B. Fischer, F. Westermeier, M. A. Schroer, Y. Chushkin, C. Gutt, M. Sprung, and G. Grubel, Phys Rev E Stat Nonlin Soft Matter Phys **91**, 042309 (2015).

[19] S. Busch, T. H. Jensen, Y. Chushkin, and A. Fluerasu, Eur Phys J E Soft Matter **26**, 55 (2008).

[20] W. R. Burghardt, M. Sikorski, A. R. Sandy, and S. Narayanan, Phys Rev E Stat Nonlin Soft Matter Phys **85**, 021402 (2012).

[21] F. Westermeier, D. Pennicard, H. Hirsemann, U. H. Wagner, C. Rau, H. Graafsma, P. Schall, M. P. Lettinga, and B. Struth, Soft Matter **12**, 171 (2016).

[22] K. Tamasaku, Y. Tanaka, M. Yabashi, H. Yamazaki, N. Kawamura, M. Suzuki, and T. Ishikawa, Nucl Instrum Meth A **467**, 686 (2001).

[23] B. J. Berne and R. Pecora, *Dynamic light scattering: with applications to chemistry, biology, and physics* (Wiley, New York, 1976).

[24] A. Fluerasu, A. Moussaid, P. Falus, H. Gleyzolle, and A. Madsen, J, Synchrotron Radiat **15**, 378 (2008).

[25] G. G. Fuller, J. M. Rallison, R. L. Schmidt, and L. G. Leal, J Fluid Mech **100**, 555 (1980).

[26] In ideal case that the shear rate is homogeneous in the gap, the shear rate applied to the sample can be estimated as V/d where d is the gap width. In the present case ($V = 0.10\ \mu\mathrm{m\ s}^{-1}$), calculated $V/d = 0.58 \times 10^{-3}$ s^{-1} is smaller than $\dot{\gamma} = 0.95 \times 10^{-3}\ \mathrm{s}^{-1}$ determined by XPCS analysis. For the other shear rates, V/d tended to be smaller than $\dot{\gamma}$. These discrepancies may be interpreted by non-uniform velocity field under shear due to complex phenomena, such as shear banding or slip.

[27] G. Brown, P. A. Rikvold, M. Sutton, and M. Grant, Physical Review E **56**, 6601 (1997).

[28] A. Malik, A. R. Sandy, L. B. Lurio, G. B. Stephenson, S. G. J. Mochrie, I. McNulty, and M. Sutton, Physical Review Letters **81**, 5832 (1998).

[29] A. Duri and L. Cipelletti, Europhysics Letters (EPL) **76**, 972 (2006).

[30] P. Mayer, H. Bissig, L. Berthier, L. Cipelletti, J. P. Garrahan, P. Sollich, and V. Trappe, Phys Rev Lett **93**, 115701 (2004).

[31] A. Duri, H. Bissig, V. Trappe, and L. Cipelletti, Phys Rev E Stat Nonlin Soft Matter Phys **72**, 051401 (2005).

[32] L. Berthier, G. Biroli, J.-P. Bouchaud, L. Cipelletti, and W. van Saarloos, *Dynamical Heterogeneities in Glasses, Colloids, and Granular Media, Chap. 4* (Oxford University Press, Oxford, 2011).

[33] V. Trappe, E. Pitard, L. Ramos, A. Robert, H. Bissig, and L. Cipelletti, Phys Rev E Stat Nonlin Soft Matter Phys **76**, 051404 (2007).

[34] (μ, ν) are $(0.15 \pm 0.04, 0.83 \pm 0.14)$, $(0.23 \pm 0.07, 0.75 \pm 0.15)$, $(0.23 \pm 0.07, 0.70 \pm 0.13)$, and $(0.21 \pm 0.06, 0.69 \pm 0.13)$ at $q_{\perp} = 8.76 \times 10^{-2}$, 9.25×10^{-2}, 10.26×10^{-2}, and $10.76 \times 10^{-2}\ \mathrm{nm}^{-1}$, respectively

[35] A. Madsen, R. L. Leheny, H. Guo, M. Sprung, and O. Czakkel, New Journal of Physics **12**, 055001 (2010).

[36] D. Orsi, L. Cristofolini, G. Baldi, and A. Madsen, Phys Rev Lett **108**, 105701 (2012).

FIG. 1. Schematic illustration of the experimental setup. A sample of silica particles dispersed in PVAc, sandwiched between a silicon substrate and a cylindrical rod, was irradiated at the center, where the substrate and cylindrical surface were closest. The scattered x-rays were detected downstream.

FIG. 2. Normalized time autocorrelation functions $[g_2 - 1]/\beta$ (symbols) measured at (a) $q = 4.25 \times 10^{-2}$ nm^{-1}, (b) $q = 7.26 \times 10^{-2}$ nm^{-1}, and (c) $q = 10.77 \times 10^{-2}$ nm^{-1}. Black lines: fitting curves for $[g_2(q_\perp, t) -]/\beta$ from Eq. (8), red lines: fitting curves for $[g_2(q_{//}, t) - 1]/\beta$ from Eq. (9). Blue dashed lines: the calculated $[\left|g_{1,\mathrm{S}}(q_{//}, t)\right|^2 - 1]/\beta$ with $\dot{\gamma} = 0.95 \times 10^{-3}$ s^{-1}.

FIG. 3. (a) Normalized time autocorrelation functions (symbols) measured at $q_\perp = 9.76 \times 10^{-2}$ nm^{-1} for various shear rates $\dot{\gamma}$ and the normalized time autocorrelation functions measured at $q_{//} = 9.76 \times 10^{-2}$ nm^{-1} for $\dot{\gamma} = 0$ s^{-1}. Solid lines: fitting curves from Eq. (8). (b) Plots of obtained values of Γ for various values of $\dot{\gamma}$. Dashed lines: fitting curves using $\Gamma \propto q$.

FIG. 4. $\dot{\gamma}$-dependence of A^{-1}, obtained from $q_\perp$-dependence of Γ for various $\dot{\gamma}$.

FIG. 5. Temporal fluctuation of time autocorrelation functions $C_I(q, t_1, \varDelta t)$ at $q_\perp = 9.76 \times 10^{-2}$ nm^{-1} for (a) $\dot{\gamma} = 0.90 \times 10^{-3}$, (b) 1.48×10^{-3}, (c) 2.42×10^{-3}, and (d) 3.79×10^{-3} s^{-1}. Red arrows represent the typical relaxation time for each $\dot{\gamma}$.

FIG. 6. Normalized variance of C_I at $q_\perp = 9.76 \times 10^{-2}$ nm^{-1} for various values of $\dot{\gamma}$.

FIG. 7. (a) $\dot{\gamma}$-dependence of χ^* at $q_\perp = 9.76 \times 10^{-2}$ nm^{-1}. Solid line: fitting curve $\chi^* \propto \dot{\gamma}^{-\mu}$. (b) $\dot{\gamma}$-dependence of τ^* at $q_\perp = 9.76 \times 10^{-2}$ nm^{-1}. Solid line: fitting curve $\tau^* \propto \dot{\gamma}^{-\nu}$.

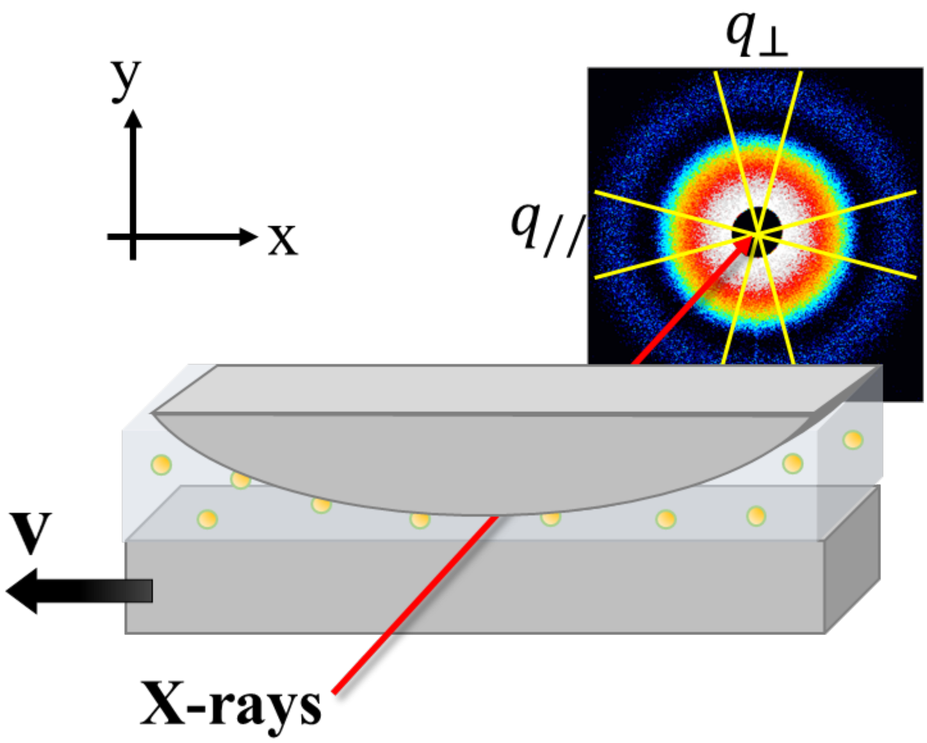

FIG. 1. Schematic illustration of the experimental setup. A sample of silica particles dispersed in PVAc, sandwiched between a silicon substrate and a cylindrical rod, was irradiated at the center, where the substrate and cylindrical surface were closest. The scattered x-rays were detected downstream.

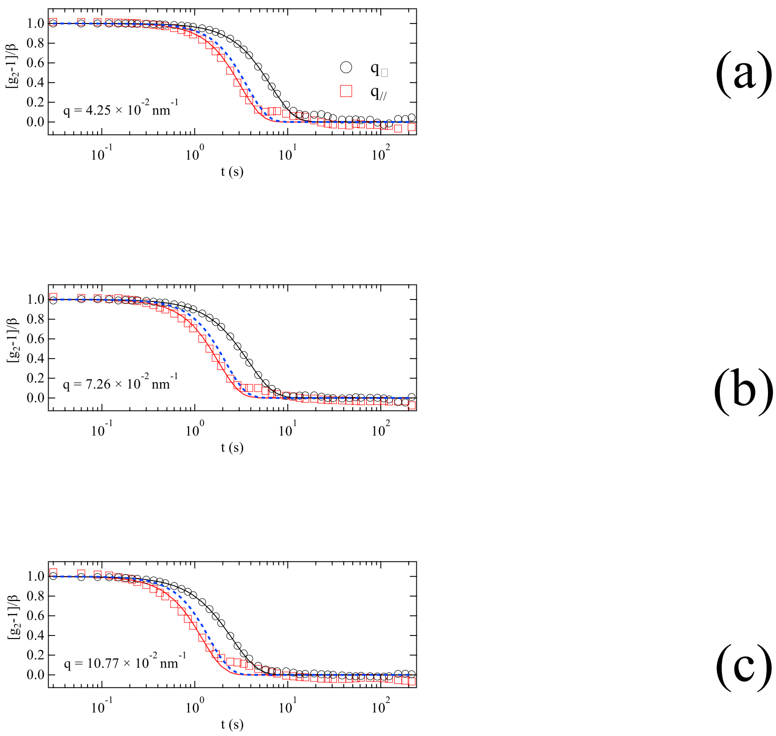

FIG. 2. Normalized time autocorrelation functions $[g_2 - 1]/\beta$ (symbols) measured at (a) $q = 4.25 \times 10^{-2}\ \mathrm{nm}^{-1}$, (b) $q = 7.26 \times 10^{-2}\ \mathrm{nm}^{-1}$, and (c) $q = 10.77 \times 10^{-2}\ \mathrm{nm}^{-1}$. Black lines: fitting curves for $[g_2(q_\perp, t) -]/\beta$ from Eq. (8), red lines: fitting curves for $[g_2(q_{//}, t) - 1]/\beta$ from Eq. (9). Blue dashed lines: the calculated $[|g_{1,S}(q_{//}, t)|^2 - 1]/\beta$ with $\dot{\gamma} = 0.95 \times 10^{-3}\ \mathrm{s}^{-1}$.

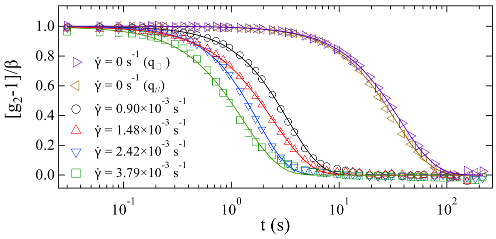

(a)

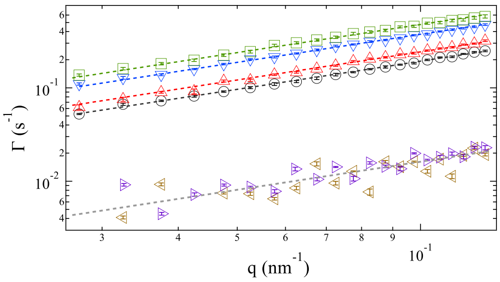

(b)

FIG. 3. (a) Normalized time autocorrelation functions (symbols) measured at $q_{\perp} = 9.76 \times 10^{-2}\ \mathrm{nm}^{-1}$ for various shear rates $\dot{\gamma}$ and the normalized time autocorrelation functions measured at $q_{//} = 9.76 \times 10^{-2}\ \mathrm{nm}^{-1}$ for $\dot{\gamma} = 0$ s-1. Solid lines: fitting curves from Eq. (8). (b) Plots of obtained values of Γ for various values of $\dot{\gamma}$. Dashed lines: fitting curves using $\Gamma \propto q$.

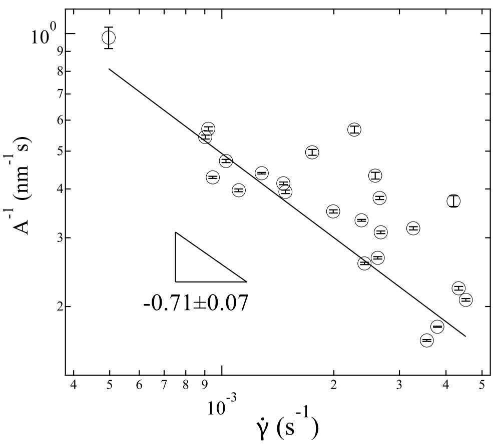

FIG. 4. $\dot{\gamma}$-dependence of A^{-1}, obtained from $q_{\perp}$-dependence of Γ for various $\dot{\gamma}$.

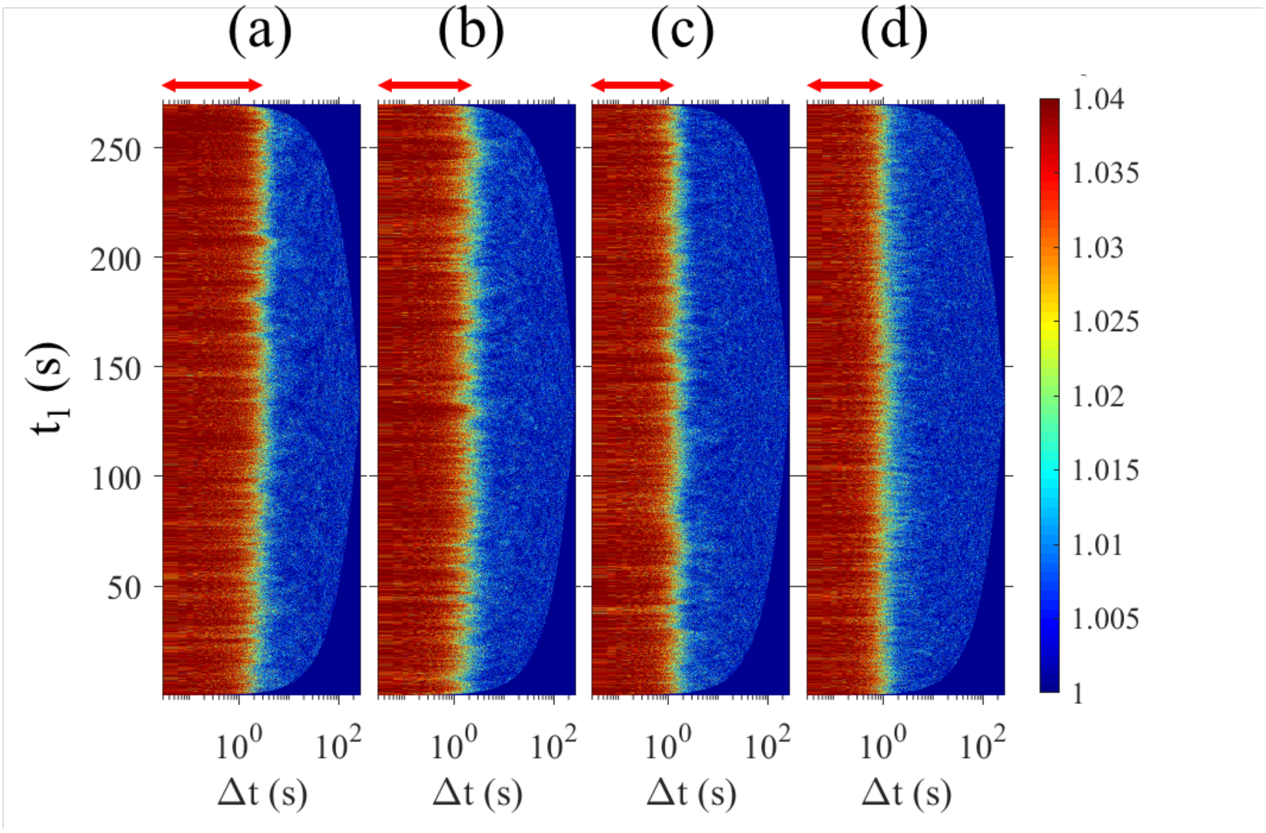

FIG. 5. Temporal fluctuation of time autocorrelation functions $C_I(q, t_1, \Delta t)$ at $q_\perp = 9.76 \times 10^{-2}\ \mathrm{nm}^{-1}$ for (a) $\dot{\gamma} = 0.90 \times 10^{-3}$, (b) 1.48×10^{-3}, (c) 2.42×10^{-3}, and (d) $3.79 \times 10^{-3}\ \mathrm{s}^{-1}$. Red arrows represent the characteristic relaxation time for each $\dot{\gamma}$.

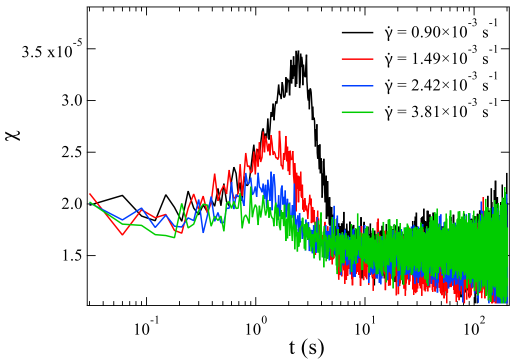

FIG. 6. Normalized variance of C_I at $q_\perp = 9.76 \times 10^{-2}\ \mathrm{nm}^{-1}$ for various values of $\dot{\gamma}$.

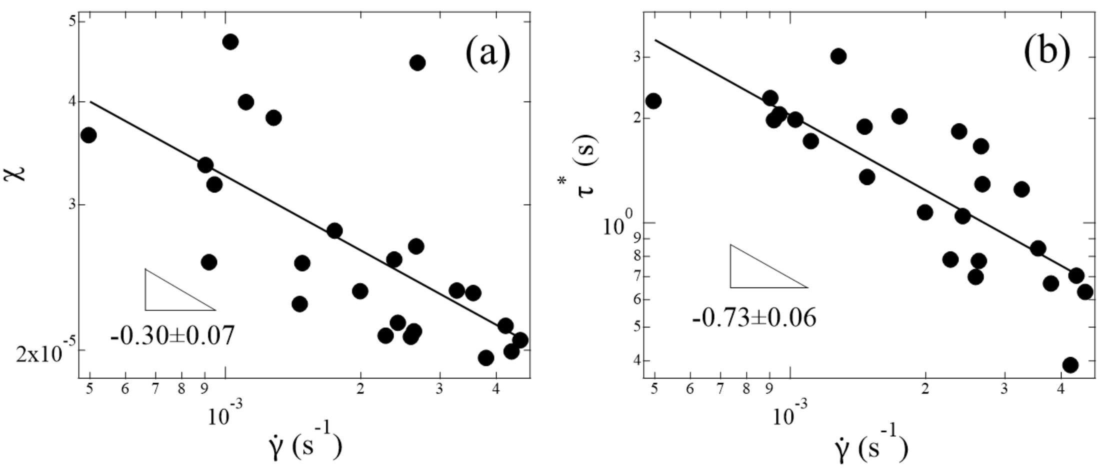

FIG. 7. (a) $\dot{\gamma}$-dependence of χ^* at $q_\perp = 9.76 \times 10^{-2}\ \mathrm{nm}^{-1}$. Solid line: fitting curve $\chi^* \propto \dot{\gamma}^{-\mu}$. (b) $\dot{\gamma}$-dependence of τ^* at $q_\perp = 9.76 \times 10^{-2}\ \mathrm{nm}^{-1}$. Solid line: fitting curve $\tau^* \propto \dot{\gamma}^{-\nu}$.